AMERICAN ACADEMY OF OPHTHALMOLOGY®

In Vivo Retinal Pigment Epithelium Imaging using Transscleral Optical Imaging in Healthy Eyes

Laura Kowalczuk, PhD,[1,2,3] *Rémy Dornier,*[1] *Mathieu Kunzi,*[1] *Antonio Iskandar, MD,*[2,3] *Zuzana Misutkova, MD,*[2,3] *Aurélia Gryczka,*[2,3] *Aurélie Navarro,*[2,3] *Fanny Jeunet,*[2,3] *Irmela Mantel, MD,*[2,3] *Francine Behar-Cohen, MD, PhD,*[4,5,6,7,8] *Timothé Laforest, PhD,*[1] *Christophe Moser, PhD*[1]

Objective: To image healthy retinal pigment epithelial (RPE) cells in vivo using Transscleral OPtical Imaging (TOPI) and to analyze statistics of RPE cell features as a function of age, axial length (AL), and eccentricity.

Design: Single-center, exploratory, prospective, and descriptive clinical study.

Participants: Forty-nine eyes (AL: 24.03 ± 0.93 mm; range: 21.9−26.7 mm) from 29 participants aged 21 to 70 years (37.1 ± 13.3 years; 19 men, 10 women).

Methods: Retinal images, including fundus photography and spectral-domain OCT, AL, and refractive error measurements were collected at baseline. For each eye, 6 high-resolution RPE images were acquired using TOPI at different locations, one of them being imaged 5 times to evaluate the repeatability of the method. Follow-up ophthalmic examination was repeated 1 to 3 weeks after TOPI to assess safety. Retinal pigment epithelial images were analyzed with a custom automated software to extract cell parameters. Statistical analysis of the selected high-contrast images included calculation of coefficient of variation (CoV) for each feature at each repetition and Spearman and Mann−Whitney tests to investigate the relationship between cell features and eye and subject characteristics.

Main Outcome Measures: Retinal pigment epithelial cell features: density, area, center-to-center spacing, number of neighbors, circularity, elongation, solidity, and border distance CoV.

Results: Macular RPE cell features were extracted from TOPI images at an eccentricity of 1.6° to 16.3° from the fovea. For each feature, the mean CoV was $< 4\%$. Spearman test showed correlation within RPE cell features. In the perifovea, the region in which images were selected for all participants, longer AL significantly correlated with decreased RPE cell density (R Spearman, Rs $= -0.746$; $P < 0.0001$) and increased cell area (Rs $= 0.668$; $P < 0.0001$), without morphologic changes. Aging was also significantly correlated with decreased RPE density (Rs $= -0.391$; $P = 0.036$) and increased cell area (Rs $= 0.454$; $P = 0.013$). Lower circular, less symmetric, more elongated, and larger cells were observed in those > 50 years.

Conclusions: The TOPI technology imaged RPE cells in vivo with a repeatability of $< 4\%$ for the CoV and was used to analyze the influence of physiologic factors on RPE cell morphometry in the perifovea of healthy volunteers.

Financial Disclosure(s): Proprietary or commercial disclosure may be found after the references.

Supplemental material available at www.ophthalmologyscience.org.

The retinal pigment epithelium (RPE), strategically located between the photoreceptors and the choroidal circulation, forms the outer blood−retinal barrier that contributes to the health and function of photoreceptor cells.[1] Retinal pigment epithelium cells are primarily affected in age-related macular degeneration,[2] impaired in the early stages of diabetic retinopathy,[3,4] and are at the center of pathologic processes associated with pachychoroid spectrum diseases.[5] Histopathology studies in human eyes have identified RPE cell features and morphologic changes that occur with aging,[6-14] and others that are specific to the onset and progression of retinal diseases, such as age-related macular degeneration[15,16] and retinitis pigmentosa.[17] However, to date, no imaging tool is available in the clinic to image RPE cells in a simple and reliable manner, neither for early diagnosis nor for the follow-up of patients with retinal diseases. Although retinal imaging systems including OCT[18] and fundus autofluorescence (AF)[19] have revolutionized diagnosis and management of retinal diseases, allowing for the longitudinal observation of the

https://doi.org/10.1016/j.xops.2022.100234
ISSN 2666-9145/22

retinal structure and the patterns of endogenous retinal fluorophores, their low lateral resolution hinders visualization of the RPE at the cellular level.

The first in vivo images of a human RPE mosaic were obtained with adaptive optics (AOs)-scanning laser ophthalmoscope (SLO) in regions where cones were missing in a patient with cone−rod dystrophy.[20] Indeed, even if RPE cells are larger than photoreceptors and have strong light-scattering properties because of their pigments, when using *en face* illumination, RPE cells are masked by the high reflectivity of the cones because of the optical Stiles-Crawford effect.[21] The only commercially available AO camera that uses *en face* flood-illumination (rtx1™ camera, Imagine Eyes) provides high-resolution retinal images down to the photoreceptors, but poor visualization of RPE cells. Noninvasive optical imaging methods combining AO-SLO with short-wavelength AF have been used for visualization of RPE cells in the living human eye,[22] but their clinical development has been limited by safety concerns associated with AF techniques. Reflectance imaging such as dark-field AO-SLO imaging is safer,[23] but the quality of RPE images is reduced. Adaptive optics OCT, offering micrometer-level axial resolution,[24,25] combined with organelle motion was proposed as a new contrast system to visualize RPE cells.[26] However, the time required for acquisition of these dynamic images makes it uncomfortable for patients and difficult to use. Combined with infrared or near-infrared (NIR) AF, enhanced with indocyanin green, or in multimodal setups, AO-SLO successfully identified the RPE mosaic in healthy volunteers[27-31] and patients.[31,32] However, AF-based imaging methods generate significantly long-lasting AF reduction at exposures lower than those imposed by safety norms.[33] Hence, despite methodologic improvements, RPE visualization remains hindered by safety concerns and relatively long acquisition times.[34]

Transscleral OPtical Imaging (TOPI) was developed to overcome these limitations. The unconventional, transscleral illumination of the ocular fundus provides high-contrast images of the retinal layers up to the RPE, at a cellular resolution and over a large field of view (FOV) (5° × 5°).[35] Oblique illumination avoids the large background light caused by the high reflectivity of cone photoreceptors, providing a unique way to obtain high-resolution images of RPE cells.[35]

A prototype for clinical use was designed with an acquisition time of > 10 seconds. This prototype was used in a single-center, exploratory, prospective, descriptive clinical study to image RPE cells in healthy eyes with variable axial lengths (ALs) from a significant number of participants with different ages to quantify RPE morphologic features and to assess safety and repeatability of TOPI imaging.

Methods

This study (ClinicalTrials.gov: NCT04398394; kofam.ch: SNCTP000003921) was designed in accordance with the tenets of the Declaration of Helsinki, good clinical practice defined by the International Council for the Harmonization of Technical Requirements for the Registration of Pharmaceuticals for Human Use, or the ISO 14155, as well as all national legal and regulatory requirements. The Ethics Committee of the Swiss Federal Department of Health approved the study (Authorization CER-VD no. 2019-00429).

Written informed consent was received from all participants before inclusion. Healthy volunteers > 18 years old were included between the period of August 2020 and December 2020 at Jules-Gonin Eye Hospital. Only healthy eyes, emmetropic or ametropic between + 3 diopters (D) and −6D, presenting with normal fundus examination, were included. Exclusion criteria included eyes with opacity of the anterior segment or other abnormality preventing good visualization of the fundus, eyes with any ocular disease, or in one of the following clinical situations: < 3 months after surgery of the anterior segment (e.g., cataract), eyes with strong myopia (< −6D), strong hypermetropia (> + 5D), and strong astigmatism (> + 4D). Not included were also individuals unable to follow the procedures of the study (for example: because of language problems, psychological disorders, dementia), individuals unable to fix a target ≥ 20 seconds, individuals not tolerant of being in the dark for 30 minutes, individuals with epilepsy, individuals with albinism, and participants refusing to be informed of the incidental discovery of a clinically significant pathology.

Clinical Examinations

Baseline examination included a standard ophthalmic examination, with best-corrected visual acuity (BCVA), intraocular pressure (IOP, Icare IC100 TA011, Medilas AG/Icare), spherical equivalent refractive error (RE) (NIDEK RT-6100, NIDEK CO), and AL (IOL MASTER 700, Carl Zeiss Meditec AG) measurements, color, AF fundus photography on the Optos ultrawide-field camera (Optos Daytona P200T), and spectral-domain OCT (serial spectral-domain OCT, 20° × 20° 193-B-scans horizontal and vertical grids) on Spectralis (Heidelberg Engineering). During this examination, an ophthalmologist (I.M.) ensured the absence of ophthalmic exclusion criteria.

Safety evaluation included a follow-up visit scheduled between 1 and 3 weeks after TOPI examination to exclude any occurrence of adverse events. It included eye examination with BCVA, IOP measurements, and eye fundus and posterior retina examinations with Optos camera and spectral-domain OCT, using the follow-up mode on Spectralis. In addition to demographic data (sex and age), eye-related clinical data were collected, including BCVA, AL, and spherical equivalent RE.

In Vivo RPE Imaging

Principle of the Modality. The details of TOPI are fully described in the article published by Laforest et al.[35] In brief, transscleral illumination of the retina is performed using 2 NIR light-emitting diodes (wavelength, λ = 850 nm, pulse peak power = 250 mW per light-emitting diode (LED), pulse duration = 8 ms, repetition rate = 11 Hz) located on the nasal and temporal side of the eye, coupled with an AO loop including a wavefront sensing (continuous illumination λ = 756 nm, peak power = 70 μW, maximum duration = 1800 seconds) embedded in our retina camera prototype. Transscleral illumination provides a large oblique beam, which is scattered by the eye fundus. In short, the infrared light is first transmitted through the sclera to the posterior segment. After reaching the retina and RPE, light propagates through the choroid and sclera, which are 2 tissues with strong scattering properties.[36] Part of the light then travels back toward the RPE, propagates through the neuroretinal translucent cells, the vitreous humor, and the lens, and is collected through the pupil.

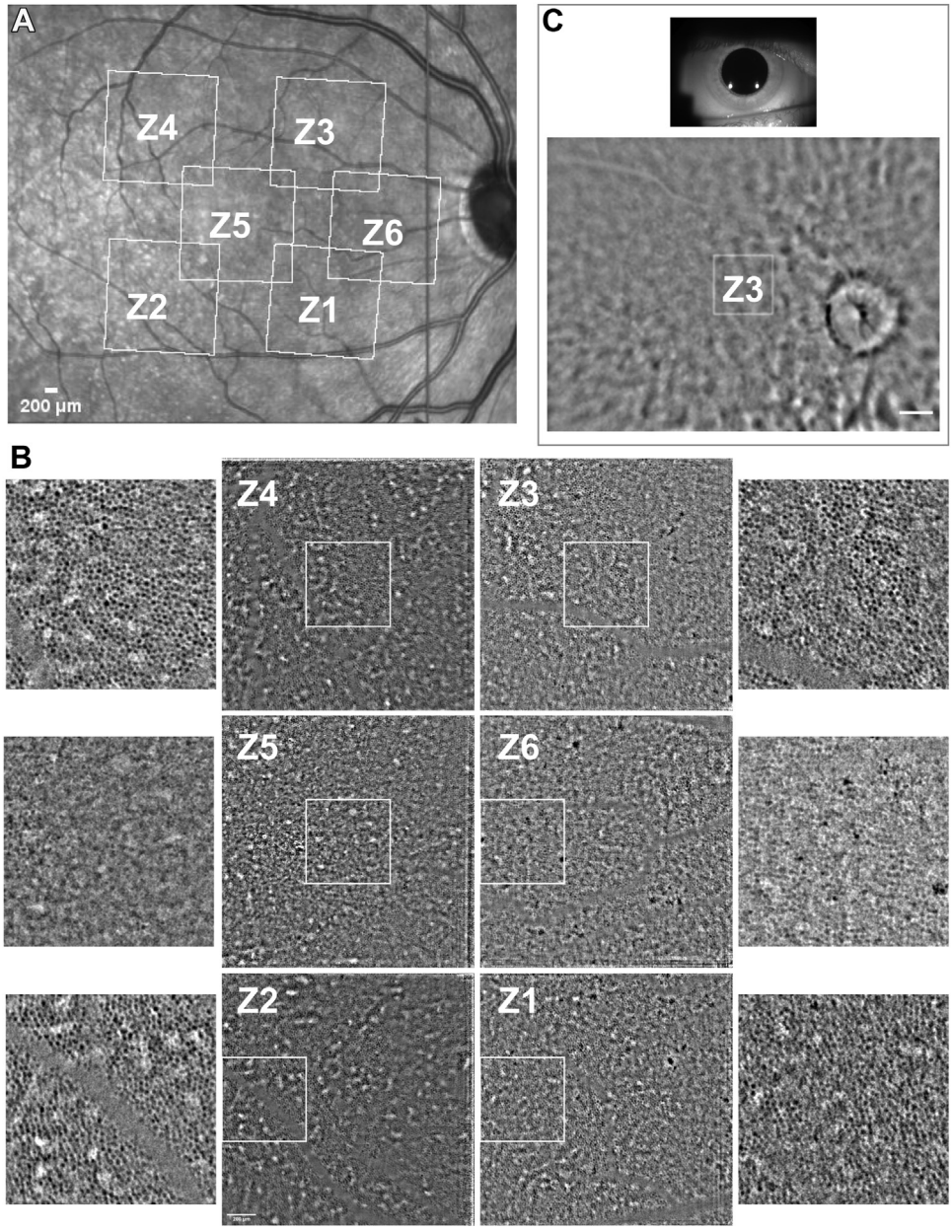

Figure 1. Locations of the in vivo retinal pigment epithelium images in the right eye of P029 (male, 29 years). **A**, Spectralis infrared right eye fundus showing the 6 imaged zones. **B**, in vivo retinal pigment epithelial images in 6 areas (Z1: inferonasal; Z2: inferotemporal; Z3: superonasal; Z4: superotemporal; Z5: foveal center; Z6: nasal). For each 5° × 5° raw image, 1 1.6° × 1.6° subimage with flat-field correction is magnified. **C**, Example of iris pictures and low-resolution oblique-illuminated 30° × 30° infrared fundus recorded during Z3 examination. Scale bars = 200 µm.

Between a depth of 250 and 350 µm, the sclera behaves as an isotropic scatterer.[36] The light is backscattered toward the RPE, which is essentially a secondary light source illuminating the RPE cells from below, which contributes greatly to the contrast of the RPE signal. The latter also contains a smaller reflection component. In the ideal case, in which AO correction implemented in our system provides diffraction-limited imaging (Rayleigh criterion),[37] while considering a 6-mm pupil diameter at 850 nm, one gets a theoretical lateral and axial resolution of approximately 3 µm and 60 µm, respectively. With unavoidably imperfect AO correction, the resolution is expected to be lower in our measurements.

Image Acquisition. For each acquisition, 100 raw images are captured in 10 seconds (10 frames per second, 8 ms pulse duration per raw image). The 100 raw images are then aligned and averaged to produce a single high signal-to-noise ratio image. Some features seem more or less contrasted on the dark-field images generated by each illumination beam; therefore, the 2 transscleral beams are used simultaneously. On the operating software graphical user interface, 5 buttons corresponding to the 5 predefined zones are used to systematically select the imaged area. Alternatively, the operator can click anywhere on the drawing representing the wide-field fundus to freely choose an area to image. These 2 actions lead to moving the internal fixation target to a specific position (Fig S1,

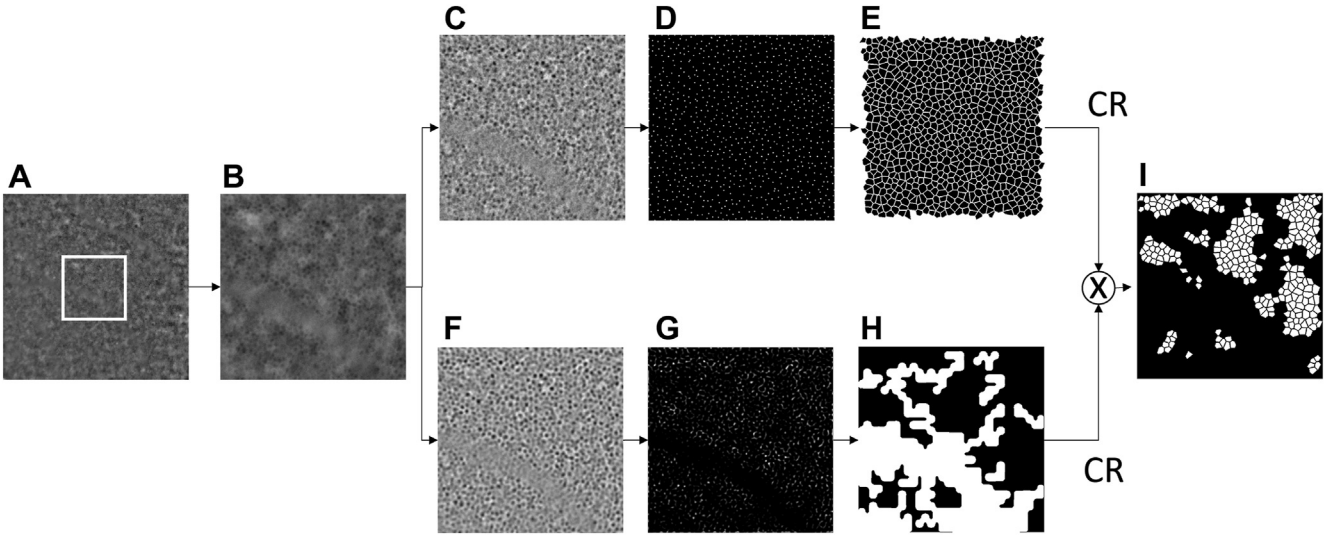

Figure 2. Image processing pipeline. First step: each 5° × 5° raw retinal pigment epithelium image (**A**) is divided into 9 1.6° × 1.6° subimages (**B**). Each subimage is then processed by 2 subpipelines running in parallel. **C**–**E**, "Segmentation subpipeline": (**C**) High-pass filtered image using an flat-field correction (FFC) with sigma = 10. **D**, Centers found using the Difference of Gaussians filter with $sigma_1 = 5$ and $sigma_2 = 10$. **E**, Voronoi-based cell segmentation. **F**–**H** "Vessel and haze detection subpipeline": **F**, High-pass filtered image using an FFC with sigma = 3.1. **G**, High-pass filtered image using Butterworth filter (cutoff frequency w = 80 pix^{-1}). **H**, Vessel and haze mask. Final step: The mask of segmented cells (**I**) is generated by removing the vessels and haze mask (**H**) from the segmentation (**E**). CR = Contrast reversing.

available at www.ophthalmologyscience.org). The foveal center is thus defined as the preferred retinal locus (PRL) of fixation, and then the internal fixation target guides the subject's gaze to select the imaged area at the defined eccentricities. When the target is centered, the imaging zone coincides with the PRL. When the target is moved, the eye rotates and remains centered on the fovea. As a result, the imaging zone is shifted away from the fovea.

Retinal pigment epithelium imaging was performed on the day of the screening visit. Three different operators (A.I., A.N., and F.J.) were involved in the image acquisition. The complete acquisition of an eye (Z1 to Z6) was performed by the same operator. In each included eye, 5 high-resolution 5° × 5° RPE images were acquired (Figure 1A, B): 4 images equidistant from the fovea at an eccentricity of 5.37° (Z1: inferonasal, Z2: inferotemporal; Z3: superonasal; Z4: superotemporal) and 1 image centered on the fovea (Z5). In some eyes, 1 additional image (Z6) was taken at the discretion of the investigator. One of the 6 zones was imaged 5 times to evaluate repeatability for a total of 10 images per eye. For each acquisition, the software records the iris image to check the alignment of the eye and a low-resolution oblique-illuminated 30° × 30° infrared fundus to locate the high-resolution RPE image (Figure 1C). The system also records the internal fixation target coordinates as described in Figure S2 (available at www.ophthalmologyscience.org). The full TOPI examination, including all the steps performed from the time the participant was greeted to the time he or she left after both eyes were imaged, lasted between 30 and 60 minutes.

RPE Image Processing and Selection

The image processing pipeline, coded in Matlab language (MATLAB (2019), version 9.7.0.1216025 (R2019b) Update 1; The MathWorks Inc), is presented in Figure 2.

The first step of the image processing consists of dividing each 5° × 5° raw image (Figure 2A) into 9 subimages of FOV 1.6° × 1.6° (Figure 2B). The eccentricities from the fovea of the subimages are calculated using the target coordinates as the center coordinates of these raw images (Fig S2). Each subimage is then processed by 2 different subpipelines. In the "segmentation subpipeline" (Figure 2C–E), a flat-field correction removes background intensity variations in the subimages to generate a high-pass filtered image (Figure 2C). Flat-field correction subtracts from the original image the image transformed with a Gaussian blur, set with sigma = 10 pixels. This filter blurs the image with a Gaussian function that eliminates details and noise with a threshold defined by its standard deviation (SD), the sigma parameter. Cell centers are then found in the resulting high-pass filtered image by a Difference of Gaussians filter ($sigma_1 = 5$; $sigma_2 = 10$). Local maxima are considered as cell centers (Figure 2D). A Voronoi-based segmentation is finally applied to find cell boundaries, using cell centers as seed points (Figure 2E). The "vessel and haze detection subpipeline" (Figure 2F–H), the algorithm previously described,[38] is applied to remove hazy parts and vessels. The subimage is high-pass filtered using a flat-field correction with sigma = 3.1 (Figure 2F) and a first-order Butterworth filter with cutoff frequency w = 80 pix^{-1} (Figure 2G). The resulting image is processed to find parts to be filtered in the image. The final step consists of removing the binary mask (Figure 2H) from the segmentation (Figure 2E) to generate the final mask used to compute output parameters (Figure 2I).

Quality Criterion. The quality of the raw images was highly variable, ranging from poor quality because of noise or out-of-focus images to high quality in the in-focus images. In the latter, some regions revealed high-contrast RPE cells next to low-contrast regions. To quantify the quality of the RPE cell contrast, we established a "quality criterion (QC)" based on the signature of the RPE in the Fourier domain (Fig S3, available at www.ophthalmologyscience.org).

On the low-pass Fourier-transformed raw image, the spatial frequencies were radially averaged (Fig S3A). The resulting

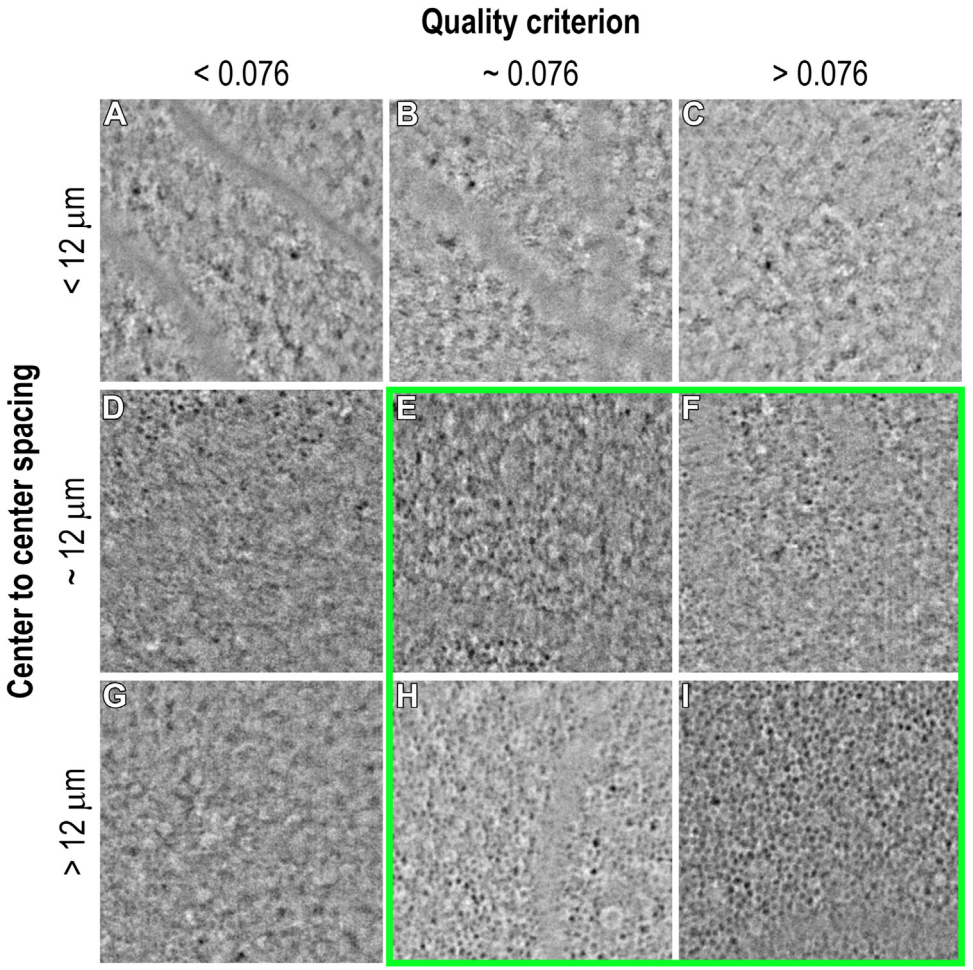

Figure 3. Illustration of the retinal pigment epithelium images selected for the statistical analysis in function of the center-to-center spacing (CCS) and the quality criterion (QC) values. Images for which the CCS was below 12 µm were excluded so as not consider other cell types or structures (**A**, CCS = 11.66 µm, QC = 0.063, left eye, from P006 [male, 27 years] at 6.6° superotemporal; **B**, CCS = 9.64 µm, QC = 0.0761, right eye from P010 [female, 32 years] at 5.37° inferotemporal; **C**, CCS = 8.95 µm, QC = 0.157, right eye from P010 at 5.83° superotemporal). Images for which the QC was < 0.076 were excluded to not consider blurry images (**D**, CCS = 11.85 µm, QC = 0.0708, right eye from P039 [male, 33 years] at 3.11° superotemporal; **G**, CCS = 13.95 µm, QC = 0.0756, left eye from P010 at 4.39° inferonasal). The green square shows examples of retinal pigment epithelium images selected for the analysis (**E**, CCS = 12.23 µm, QC = 0.0817, right eye from P017 [male, 58 years] at 5.37° inferonasal; **F**, CCS = 12.02 µm, QC = 0.128, left eye from P039 at 4.39° superonasal; **H**, CCS = 13.98 µm, QC = 0.0765 right eye from P040 [female, 31 years] at 5.83° inferonasal; **I**, CCS = 14.55 µm, QC = 0.286, right eye from P014 [female, 29 years] at 5.37° superonasal).

profile showed a positive distortion, similar to the RPE cells signature, which was not always a local maximum (Fig S3B). Because the shape and intensity of the distortion provide information about the contrast of the RPE cells in the image, 3 parameters were computed to quantify the distortion (Fig S3C): amplitude (ΔI), area (A), and gradient difference (ΔG) between both sides of the distortion. Amplitude and area were computed by interpolating a linear model between distortion's inflexion points, resulting in the "QC" cost function (Fig S3D, equation). Each parameter ΔI, A, and ΔG was normalized to take values in [0,1] without the unit and weighted to tune their influence.

Different RPE cell features were computed after segmentation: cell density (cells/mm^2), cell area (µm^2), and number of neighbor cells. On each segmented cell, the measured morphologic features (Fig S4, available at www.ophthalmologyscience.org) were circularity (a.u.), elongation (a.u.), solidity (a.u.), and border distance coefficient of variation (CoV). The center-to-center spacing (CCS) based on the Fourier signature of the cells was also computed.

To obtain the quantitative parameters, the pixel size was corrected for AL and spherical equivalent RE of the eye. Pixel size (µm) = -a*RE + b*(AL-23.5) + 0.74, where a and b come from the linear regression based on a simulation of the optical system, with different RE values and their corresponding optical magnification values (Supplemental Appendix, available at www.ophthalmologyscience.org).

Image Selection. To include only images with well-contrasted RPE cells in data analysis, the combination of 4 restricted conditions on cell features was used to select the best images (Figure 3E, F, H, I): (1) measurable "Cell density" (> 0); (2) CCS > 11.8 µm to avoid selecting images of other cell types or structures (Figure 3A–C); (3) QC > 0.076 to remove blurry and noisy images (Figure 3D, G); (4) "Number of neighboring cells" available to remove images with only isolated cells detected or

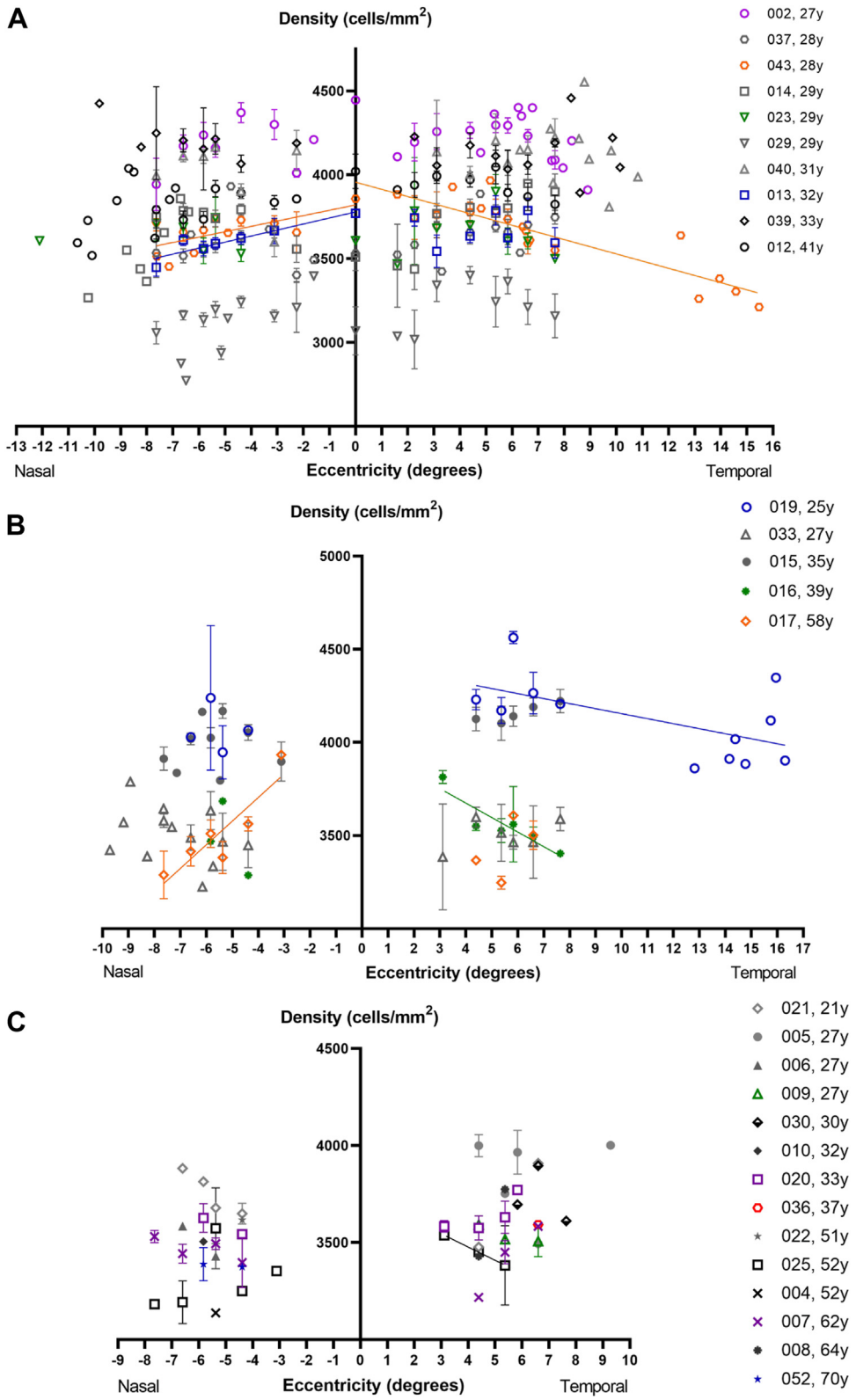

Figure 4. Average cell density for participants as a function of subimage eccentricity in the nasal and temporal regions. Each point represents the average density of the inferior and superior quadrants in each region. Data collected at X = 0 are located at 1.6° in the inferior and superior quadrants. **A**, Group 1, 10 participants with consistently selected subimages from the fovea to the perifovea. Cell density decreases with eccentricity for 1 participant (P043 [male, 28 years], orange circle) in the nasal (Y = 31.93*X + 3820; R^2 = 44.6%, P = 0.0176) and temporal regions (Y = −42.81*X + 3956; R^2 = 78.8%, $P < 0.0001$) and for 1 participant (P013 [female, 32 years], blue square) in the nasal region. **B**, Group 2, 5 participants with consistently selected subimages in the

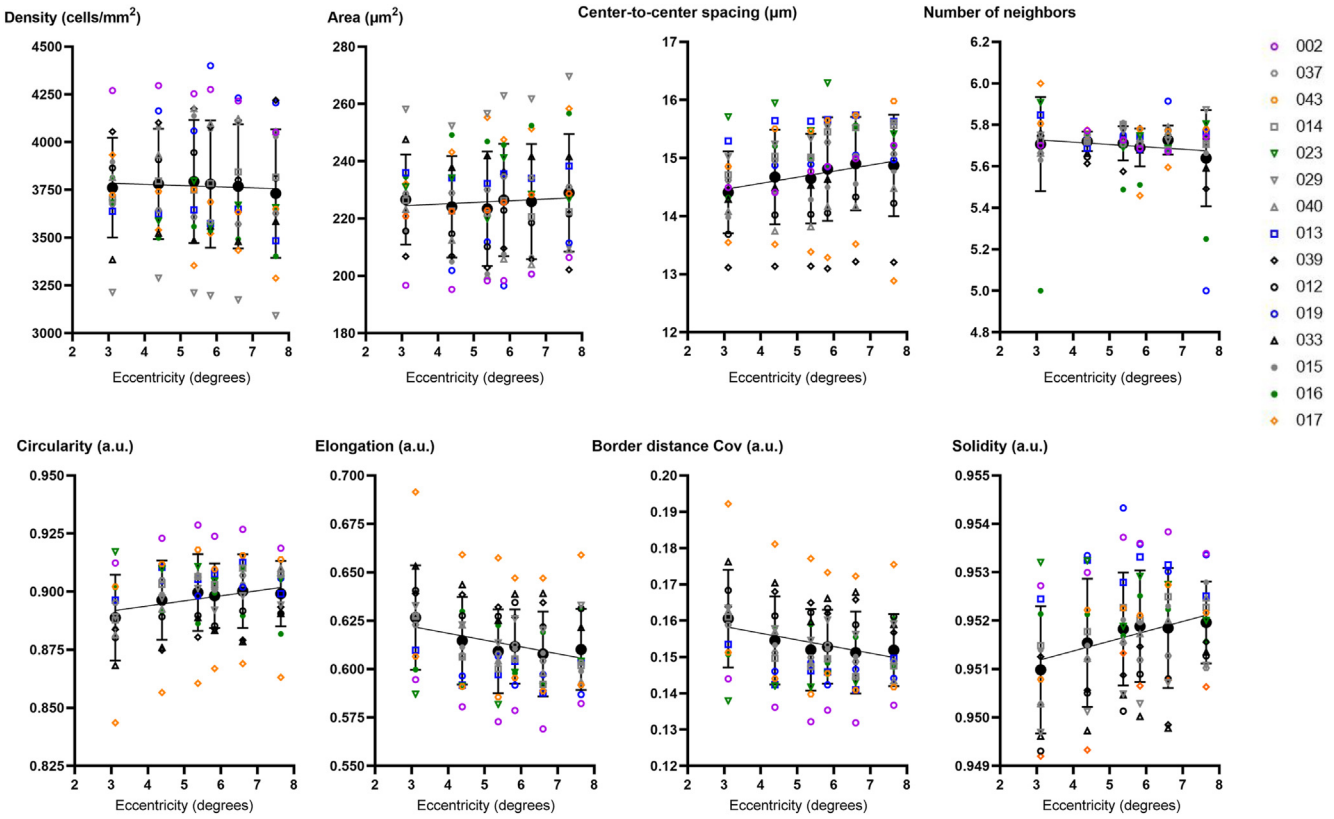

Figure 5. Linear regressions of retinal pigment epithelium cell features in function of eccentricity. Each point represents the mean ± standard deviation of average features from the 15 participants of groups 1 and 2 at each shared radial eccentricity in the perifoveal region. Between 3° and 8°, eccentricity has no influence on retinal pigment epithelium cell density ($Y = -6.194*X + 3804$; $R^2 = 0.09\%$, $P = 0.7829$), area ($Y = 0.5961*X + 222.6$; $R^2 = 0.22\%$, $P = 0.6637$), center-to-center spacing ($Y = 0.1049*X + 14.14$; $R^2 = 3.59\%$, $P = 0.0753$), number of neighbors ($Y = -0.01145*X + 5.762$; $R^2 = 1.35\%$, $P = 0.2774$), and circularity ($Y = 0.002182*X + 0.8851$; $R^2 = 3.93\%$, $P = 0.0626$) and little influence on the other morphologic features: elongation ($Y = -0.003524*X + 0.6326$; $R^2 = 5.20\%$, $P = 0.0316$; *), border distance coefficient of variation ($Y = -0.001835*X + 0.1639$; $R^2 = 5.38\%$, $P = 0.0287$; *), and solidity ($Y = 0.0002037*X + 0.9506$; $R^2 = 6.17\%$, $P = 0.0189$; *). Raw data are available in Table S5 (available at www.ophthalmologyscience.org).

with cells detected on the border. Different CCS and QC thresholds were tested, and the results were compared with the manual selection. The pair of thresholds that gave the closest selection to manual selection was kept. The CCS threshold of 11.8 µm is coherent with the published row-to-row spacing values.[24,28,31]

Data Analysis

To study the repeatability of the measurements, images of the same area were realigned with Fiji plugin "Template Matching" that corrects for translations,[39] then "TurboReg" to adjust images in rotation and translation.[40] The corrected images were then cropped to get the same area on each image, processed with the standard pipeline, and selected with the restricted conditions described above after computation of RPE cell features. The CoV of each cell feature was calculated for each repetition.

Statistical Analysis

GraphPad Prism software (version 9.1.2 [226], GraphPad Software, LLC) was used to calculate descriptive statistics of the quantitative data (eye characteristics, mean cell features per subject), to test the normal distribution of the variables (age, AL, RE, BCVA, IOP, cell features) by the Kolmogorov–Smirnov normality tests, and to run the Spearman correlation test and linear regressions. To investigate the effect of AL, age, and eccentricity, multiple comparisons of the variables (participants, eyes, and cell features) between eccentricities and groups of participants (males versus females; age < 50 years versus > 50 years) was performed with the Multiple Mann–Whitney test, corrected with the Holm–Šídák method. This nonparametric test based on the distribution of ranked values in each group does not require an equal sample size. For all statistical tests, $P < 0.05$ was considered significant.

perifovea. Cell density decreases with eccentricity for 1 participant (P017 [male, 58 years], orange diamond) in the nasal region ($Y = 126.9*X + 4211$; $R^2 = 80.7\%$, $P = 0.015$) and for 2 participants in the temporal region (P019 [female, 25 years], blue circle: $Y = -26.95*X + 4424$; $R^2 = 34.8\%$, $P = 0.0436$; P016 [male, 39 years], green dot: $Y = -77.96*X + 3986$; $R^2 = 82.4\%$, $P = 0.0124$). **C**, Group 3, 14 participants with irregularly selected images in the perifovea. Cell density decreases with eccentricity for 1 participant (P025 [male, 52 years], black square) in the temporal region ($Y = -68.27*X + 3750$; $R^2 = 99\%$, $P = 0.0119$). Raw data are available in Table S4 (available at www.ophthalmologyscience.org).

Table 1. Multiple Mann–Whitney Comparisons of the RPE Cell Features Computed from the Images Obtained between 3° and 8°, Per Sex Group

Comparison	Mean ± SD				Multiple Mann–Whitney			Holm-Šídák method	
Females versus Males	*Females*		*Males*		*P Value*	*Mean Rank Difference*	*Mann–Whitney U*	*Adjusted P Value*	*< Threshold (0.05)?*
Axial length (mm)	23.44	0.89	24.34	0.80	0.0050	-9.082	35.5	0.054	No
Mean area (μm^2)	223.3	17.5	238.1	15.3	0.0771	5.953	56	0.514	No
Cell density (cells/mm^2)	3821	292	3583	235	0.0624	-6.258	54	0.475	No
Border distance CoV (a.u.)	0.1557	0.014	0.1629	0.012	0.1507	-4.884	63	0.729	No
Circularity (a.u.)	0.8941	0.018	0.8833	0.018	0.1537	4.808	63.5	0.729	No
Solidity (a.u.)	0.9517	0.001	0.951	0.001	0.2468	3.968	69	0.817	No
SD area (μm^2)	57.91	14.18	61.09	6.56	0.3077	-3.511	72	0.841	No
Quality criterion (a.u.)	0.1251	0.036	0.1119	0.024	0.3532	3.205	74	0.841	No
Elongation (a.u.)	0.6193	0.029	0.6302	0.021	0.4026	-2.9	76	0.841	No
Age (yrs)	32.6	7.5	39.47	15.2	0.3696	-3.053	75	0.841	No
Center-to-center spacing (μm)	14.51	0.70	14.52	0.83	0.9820	-0.153	94	0.982	No

Females (n = 10 participants; axial length [AL] mean = 23.44 ± 0.88 mm, median = 23.54 mm, range 21.99-24.95 mm) *versus* males (n = 19 participants; AL mean = 24.34 ± 0.80 mm, median = 24.30 mm, range 22.7-26.61 mm). CoV = coefficient of variation; RPE = retinal pigment epithelium; SD = standard deviation.

Results

Image Selection

Forty-nine eyes presenting with good visual acuity from 29 healthy volunteers (19 males and 10 females) with a mean age of 37.1 ± 13.3 years (range, 21–70 years) were included in this study. Participant and eye data collected at visit 1, including screening and TOPI examination, and at visit 2 for safety evaluation are summarized in Table S1 (available at www.ophthalmologyscience.org). During TOPI examinations, no adverse event related to the procedure was reported. Comparisons of BCVA and IOP between both visits revealed no statistical difference (Mann–Whitney $P = 0.2917$ and 0.4419, respectively). Multimodal, slit-lamp, fundoscopy, and OCT imaging did not reveal any change on retinal structures before and after TOPI examination (Table S1).

A total of 580 raw images were acquired, which means that 5220 subimages were processed. Comparison of the average QC per eye and per operator on this initial data set showed no interoperator variability. After the automatic image selection that retained 1553 subimages, a manual check removed 47 other subimages, including those at the center of the fovea image (Z5), because no RPE cells were visible at this location (see Figure 1B, Z5 magnification) and to avoid biasing the measurement at (0°, 0°). The final analyzed dataset included 1506 high-quality and well-contrasted RPE cells images, representing 29% of the total raw subimages.

Statistics on Average RPE Cell Features

Table S2 (available at www.ophthalmologyscience.org) summarizes the number of subimages selected per participant and per eccentricity. Three groups of participants were defined on the basis of usable foveal images and frequency of usable perifoveal images. The fovea was sampled between 1.6° and 2.9° in 10 participants (group 1, Fig 4A). The perifovea was consistently sampled between 3° and 8° in 15 participants (10 in group 1; 5 in group 2; Fig 4B) and irregularly sampled in 14 participants (group 3; Fig 4C). In addition, images were taken in retinal periphery over 8° to 16.3° at the discretion of the investigator in 10 participants (7 in group 1; 2 in group 2; 1 in group 3).

Effect of Eccentricity

Figure 4 presents the average density of each participant in function of nasal and temporal eccentricities. Individual linear regressions showed significant correlations for 6 participants.

To investigate the effect of eccentricity on cell density, only the data collected at shared eccentricities of the 15 participants from groups 1 and 2 were considered. Multiple comparisons of average densities at each radial eccentricity (inferior versus superior and nasal versus temporal sides) showed no statistical difference, demonstrating that RPE cell densities are constant in the perifovea (Fig S5, available at www.ophthalmologyscience.org).

Given the radial symmetry around the fovea, the effect of eccentricity on RPE cell features in the perifovea was investigated only in function of radial eccentricity. Linear regressions of RPE cell features in function of eccentricity in the perifovea showed no effect of eccentricity on cell density, area, CCS, and circularity and that cells have a number of neighbors close to 5.7, confirming the regularity of the RPE cell between 3° and 8° (Fig 5). The morphologic features elongation ($R^2 = 5.20\%$, $P = 0.0316$), border distance CoV ($R^2 = 5.38\%$, $P = 0.0287$), and solidity ($R^2 = 6.17\%$, $P = 0.0189$) showed a slight correlation with eccentricity.

Correlation between Age, Eye Characteristics, and Cell Features

Considering that eccentricity has little influence on RPE cell characteristics over this narrow range of eccentricities, the

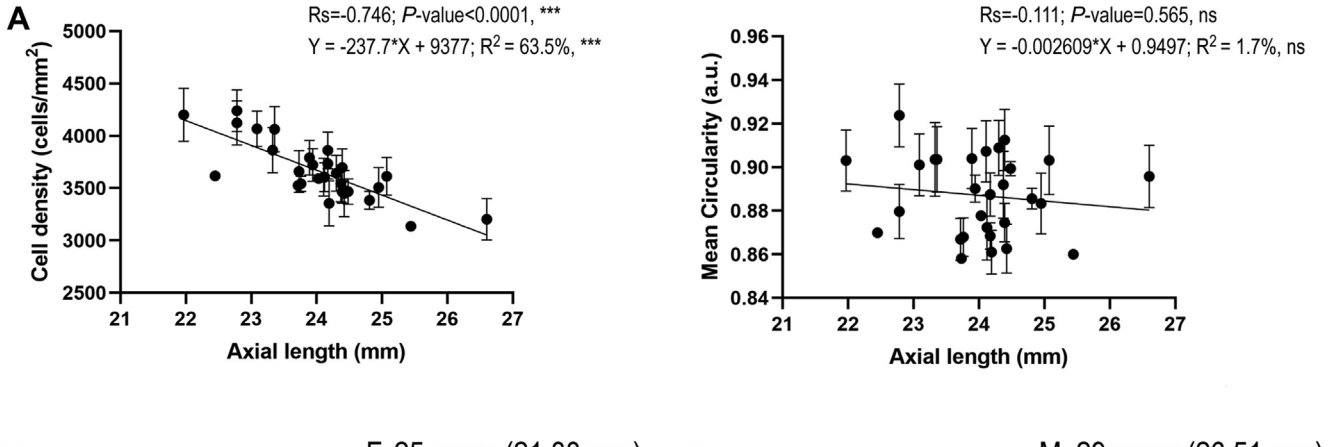

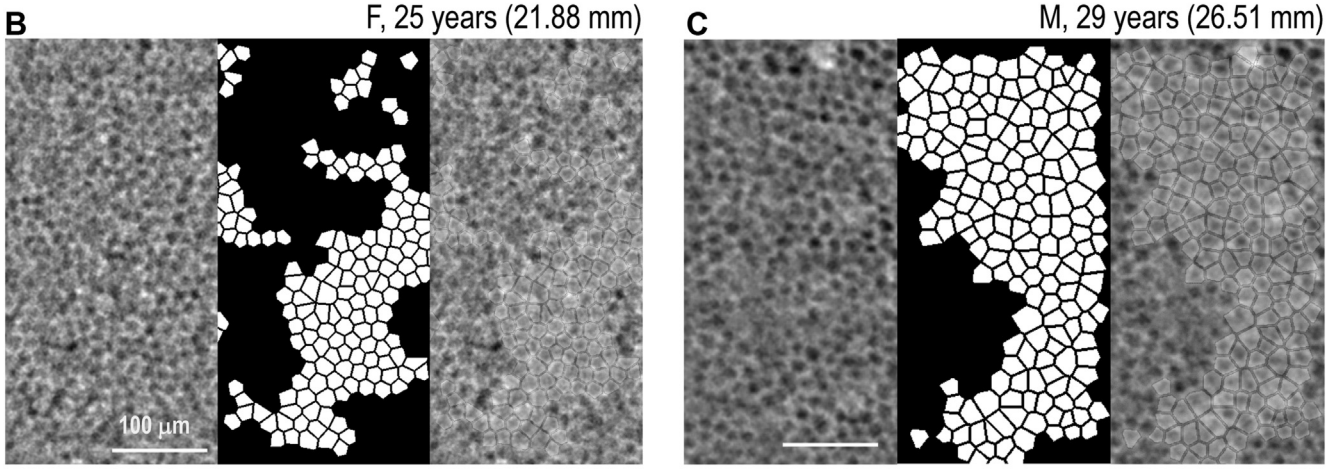

	Mean (image)	Mean (OD/OS)
Cell density (cells/mm^2)	4254	4155
Mean cell diameter (µm)	15.3	15.5
Mean area (µm^2)	196	206
Border distance Cov (a.u.)	0.13	0.14
Circularity (a.u.)	0.93	0.91
SD Area (µm^2)	34.6	45.0
Elongation (a.u.)	0.55	0.59

	Mean (image)	Mean (OD/OS)
Cell density (cells/mm^2)	3511	3194
Mean cell diameter (µm)	16.9	16.7
Mean area (µm^2)	230	237
Border distance Cov (a.u.)	0.15	0.17
Circularity (a.u.)	0.92	0.87
SD Area (µm^2)	51.7	55.2
Elongation (a.u.)	0.60	0.65

Figure 6. Effect of axial length (AL) on retinal pigment epithelium cell features. **A**, Linear regressions of AL in function of cell density and circularity. Illustration of quantification in a subimage of the shorter eye (**B**, AL = 21.88 mm, left eye from P019 [female, 25 years] at 5.37° superotemporal) versus one of the longer eyes (**C**, AL = 26.51 mm, left eye from P029 [male, 29 years] at 4.39° superotemporal). CoV = coefficient of variation; OD = right eye; OS = left eye; SD = standard deviation.

data computed from the 1397 subimages from the 29 participants between 3° and 8° were analyzed to investigate the relationship among age, eye characteristics, and cell features.

The normality test revealed that continuous variables related to patient and eye characteristics do not follow a normal distribution. Therefore, the nonparametric Spearman coefficient was used to measure correlation among participant age, eye data, and RPE cell features (Table S3).

The Spearman matrix shows that RPE cell morphologic features are correlated between them. For example, increases in elongation (mean) and border distance CoV (mean and SD) are correlated with decreases in circularity (mean and SD), solidity (mean and SD), number of neighboring cells, and density, and with an increase in cell area (mean and SD). The mean number of neighboring cells (5.7 ± 0.11; range 5.3−5.8) remains constant regardless of the age and sex of the participant and the AL of the eye. The distribution of the number of neighbors confirmed that a large majority of RPE cells have a triangular packing arrangement (Fig S6A, available at www.ophthalmologyscience.org).

Effect of AL. As expected, AL was correlated with RE (Table 1; Rs = − 0.563; P = 0.001). Considering the corrected pixel size, the cell density decreased with AL (Rs = −0.746; $P < 0.0001$). This was correlated with an increase in cell area (Rs = 0.668; $P < 0.0001$), without change in cell morphologic features, such as circularity (Figure 6A; Rs = − 0.111; P = 0.565). Linear regressions were consistent with these findings. Figure 6B

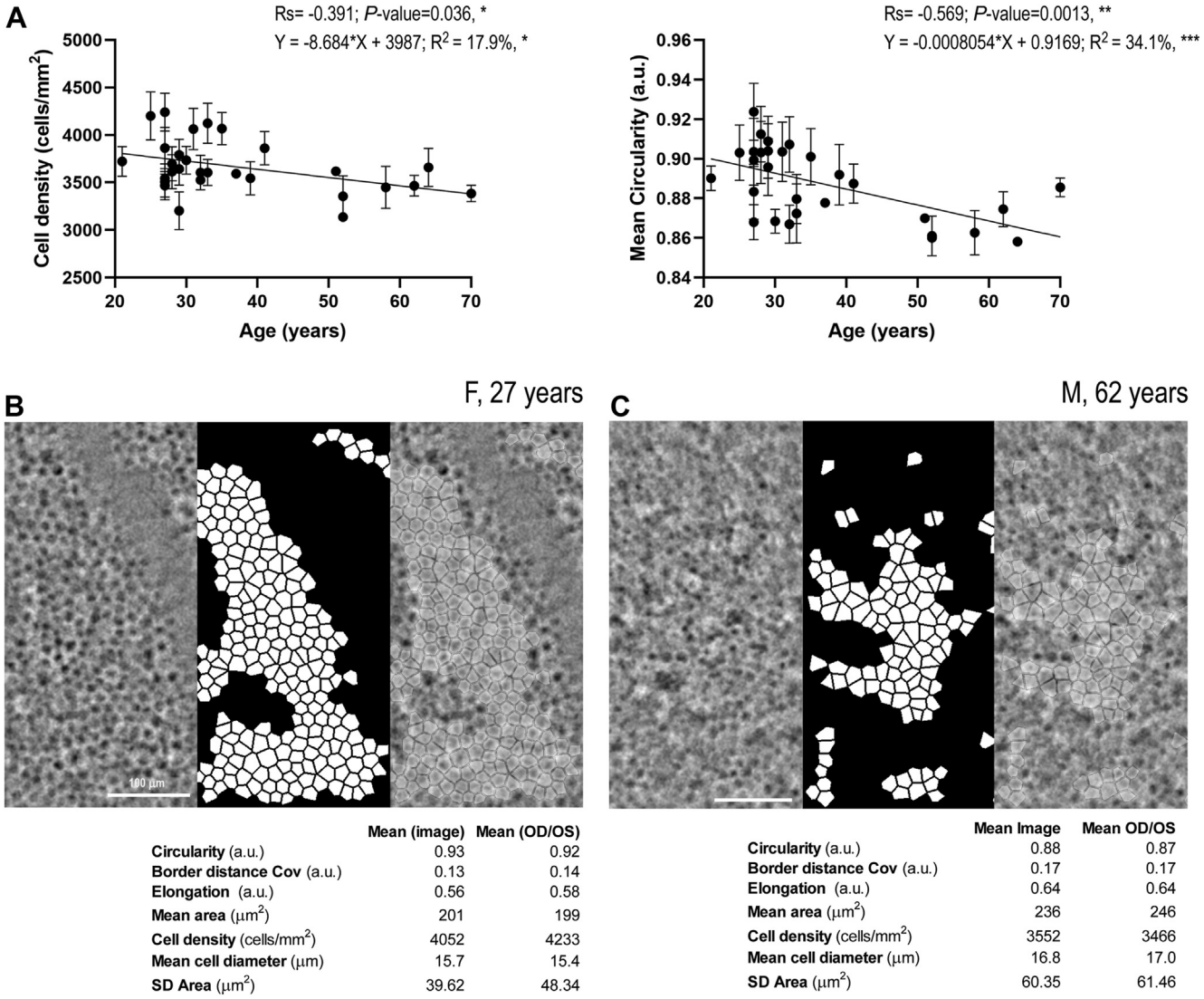

	Mean (image)	Mean (OD/OS)
Circularity (a.u.)	0.93	0.92
Border distance Cov (a.u.)	0.13	0.14
Elongation (a.u.)	0.56	0.58
Mean area (μm^2)	201	199
Cell density (cells/mm^2)	4052	4233
Mean cell diameter (μm)	15.7	15.4
SD Area (μm^2)	39.62	48.34

	Mean Image	Mean OD/OS
Circularity (a.u.)	0.88	0.87
Border distance Cov (a.u.)	0.17	0.17
Elongation (a.u.)	0.64	0.64
Mean area (μm^2)	236	246
Cell density (cells/mm^2)	3552	3466
Mean cell diameter (μm)	16.8	17.0
SD Area (μm^2)	60.35	61.46

Figure 7. Effect of age on retinal pigment epithelium cell features. (A) Linear regressions of age in function of cell density and circularity. Illustration of quantification in a subimage of one of the younger participants (**B**, 27 years, left eye from P002 [female] at 6.6° superotemporal) versus one of the older participants (**C**, 62 years, left eye from P007 [male] at 5.37° superotemporal). CoV = coefficient of variation; OD = right eye; OS = left eye; SD = standard deviation.

and C illustrates 1 image from the shortest eye (female, 25 years) compared with the longest eye (male, 29 years). The morphologic parameters show larger cells in the long eye, with a geometry similar to those of the short eye.

The mean AL of the females (n = 10 participants, 23.44 ± 0.88 mm) was significantly lower than that of the males (n = 19 participants, 24.34 ± 0.80 mm; $P = 0.0055$). Multiple comparisons showed that neither variable (age, AL, and RPE cell features) was significantly different between males and females (Table 1).

Effect of Age. A significant decrease in cell density with age was measured (Figure 7A; Rs = −0.391; $P = 0.036$), implying an increase in mean cell area (Rs = 0.454; $P = 0.013$). The shape of the RPE cells also changed with age, as demonstrated by the calculated Spearman coefficients and their related significant P values, for circularity (illustrated in Figure 7A; Rs = −0.569; $P = 0.0013$), elongation (Rs = 0.562; $P = 0.001$), solidity (Rs = −0.406; $P = 0.028$), and border distance CoV mean (Rs = 0.580; $P = 0.001$). This result is illustrated in the comparison of 1 young participant with 1 of the oldest volunteers. It shows less circular, less symmetric, elongated, and larger cells in the image of the older eye (Figure 7B, C).

To assess the effect of age on these independent variables, the cohort was divided into 2 groups: participants < 50 years and those > 50 years. The multiple nonparametric test demonstrated that the RPE cell features that significantly differed over 50 years were circularity (mean), border distance CoV (mean), elongation (mean), area (mean), and density (Table 2). The mean number of neighbors was not different between groups, but the distribution of the

Table 2. Multiple Mann–Whitney Comparison of the RPE Cell Features Computed from the Images Obtained between 3° and 8°, Per Age Group

Comparison	Mean ± SD				Multiple Mann–Whitney			Holm-Šídák method	
< 50 yrs versus > 50 yrs	*< 50 yrs*		*> 50 yrs*		*P Value*	*Mean Rank Difference*	*Mann–Whitney U*	*Adjusted P Value*	*< Threshold (0.05)?*
Circularity (a.u.)	0.8933	0.0159	0.8674	0.0099	0.0006	11.86	14	0.006	Yes
Border distance CoV (a.u.)	0.1565	0.0116	0.173	0.0058	0.0007	-11.68	15	0.007	Yes
Elongation (a.u.)	0.6189	0.0228	0.6502	0.0089	0.0012	-11.30	17	0.011	Yes
Mean area (μm^2)	227.8	16.0	249.3	9.7	0.0015	-11.11	18	0.012	Yes
Cell density (cells/mm^2)	3737	265	3438	174	0.0064	9.79	25	0.044	Yes
SD area (μm^2)	57.6	9.7	67.5	4.7	0.0109	-9.23	28	0.064	No
Center-to-center spacing (μm)	14.71	0.71	13.93	0.71	0.0279	8.10	34	0.132	No
Quality criterion (a.u.)	0.123	0.029	0.09575	0.014	0.0422	7.53	37	0.158	No
Solidity (a.u.)	0.9514	0.0013	0.9506	0.0009	0.1647	5.27	49	0.417	No
Axial length (mm)	23.97	0.94	24.2	0.94	0.3667	-3.86	57	0.482	No
Number of neighbors	5.69	0.09	5.63	0.16	0.3282	3.766	57	0.482	No

"< 50 years" (n = 22 participants; age mean = 30.3 ± 4.7 years, median = 29 years, range 21-41 years) versus "> 50 years" (n = 7 participants; age mean = 58.4 ± 7.3 mm, median = 58 years, range 51-70 years).
CoV = coefficient of variation; RPE = retinal pigment epithelium; SD = standard deviation.

average number of neighbors per subimage depended on the age group of the participants, as shown in Figure S6B (available at www.ophthalmologyscience.org). An average of 5.8 neighbors was found in 35% of the images for participants < 50 years, whereas this figure was only 20% for participants > 50 years. This suggests a rearrangement of the RPE cells with aging.

Repeatability of the Acquisition

To test the setup repeatability, the same operator under the same conditions took images of the same area a few minutes apart (Fig S7, available at www.ophthalmologyscience.org). After selection of the well-contrasted RPE images, the images taken in 25 eyes from 17 participants (10 male, 7 female; age 35.9 ± 13.8 years, range 25–70 years) were included in this analysis. Repetitions were done on the inferonasal area (Z1) for 24 eyes and on the inferotemporal area (Z2) for 1 eye, with an average number of selected images of 4.7 ± 1.4 per subject. After realignment, segmentation, and analysis of the images, the cell features were computed. The computed CoV (mean ± SD) of the mean cell features measured in the repeated areas is presented in Table 3. For each feature, the average CoV was < 4%.

Table 3. Cell Features CoV on 25 Areas, Imaged 4.7 ± 1.4 Times

Cell Features	Mean CoV	SD CoV
Cell density (cells/mm^2)	0.032	0.013
Area (μm^2)	0.035	0.016
Number of neighboring cells	0.024	0.021
Circularity (a.u.)	0.010	0.004
Elongation (a.u.)	0.023	0.011
Solidity (a.u.)	0.001	0.001
Border distance CoV (a.u.)	0.039	0.017

CoV = coefficient of variation; SD = standard deviation.

Discussion

Using TOPI, the RPE could safely be imaged in 49 eyes from 29 healthy volunteers aged 21 to 70 years over the macula between 1.6° and 16.3° eccentricity from the fovea. In all tested eyes, with a mean AL of 24.03 ± 0.93 mm (range, 21.9–26.7 mm), high-resolution images of RPE were obtained for analysis.

The previously described image analysis tool for RPE cell detection, segmentation, and quantification was used with strict criteria to select well-contrasted cells, thus removing not only the vessels area but also the blurred and low-contrast areas on the RPE cells.[38] Ideally, with our imaging modality relying on transillumination and melanin absorption, 1 RPE cell appears as a uniform black central area surrounded by a bright interface. A central area with nonuniform intensity distribution or with an intensity significantly different from that of its neighboring cells may result in poor imaging of the cell borders. This explains why the RPE cell pattern was not well resolved in some areas, even in high-quality images. The reason for such a nonideal distribution may be twofold: (1) The density of melanin pigments in the granules fluctuates and the latter are randomly distributed in the cell apical layer,[41,42] as well as between neighboring cells, resulting in a nonhomogeneous random contrast pattern that may give rise to ambiguous discrimination of cell borders; and (2) transillumination may be disturbed or attenuated by vessels or melanin granules in the choroidal layers, altering the distribution of light projected to the RPE and distorting image contrast. Our current prototype did not allow imaging the RPE cells in the center of the fovea, which prevented us from performing analyses in this area. The origin of the lower image quality in the foveal center is not yet completely clear. It might simply be because of nonoptimal focusing or due to a stronger perturbation of the transillumination mechanisms inherent to our method in the foveal area. This hypothesis is supported by the higher vascular density in

Table 4A. Summary of In Vivo RPE Cell Imaging Studies in Healthy Eyes. For Comparison, the Reported Data from the Fovea to the Periphery are Summarized

Reference	Modality	N	Age (yrs)		Axial Length (mm)		Density (cells/mm^2): Mean ± SD per Eccentricity Range				Other RPE Cell Features Reported
			Mean	*Min–Max*	*Mean*	*Min–Max*	*Foveal Pit*	*Fovea*	*Perifovea*	*Periphery*	
Current study	TOPI						**0°**	**1.6°–2.3°**	**3°–8°**	**8°–16.3°**	
		29	37.1	21–70	24.03	21.9–26.7	N/A	3770 ± 356 (n = 10)	3665 ± 276	3810 ± 312 (n = 10)	Center-to-center spacing, area, number of neighbors, circularity, elongation, border distance CoV, solidity
		22	30.3	21–41	23.97	0.94			3737 ± 265		
		7	58.4	51–70	24.2	0.94			3438 ± 311		
Laforest, 2020[35]	TOPI							**2.2°–2.7°**	**3°–8°**	**8°–12.5°**	
		11	28.8	19–49	N/A		N/A	4887 ± 454 (n = 2)	4382 ± 1114 (ns)	4063 ± 237 (ns)	Area; RRS (2°–12°): 13.8 µm
Baraas, 2022[25]	AO-SLO, AO-OCT						**0.2 × 0.2 mm** (0.7 x 0.7°)	**0.7°–6°**			
		23	31.8	15–66	23.5	20.6–25.1	7698 ± 1195 (n = 9)	N/A			RPE intercellular distance: 8–18 µm
		19	26.8	15–48	23.5	20.6–25.1	7607 ± 1114				No foveal density change with age
		4	55.8	50–66	23.6	22.2–24.6	8129 ± 1650 (n = 2)				
Bower, 2021[31]	Multimodal: AO-darkfield, AO-ICG, AO-IRAF, AO-OCT	4	29	± 11	N/A		**0 mm** ~ 7000	**0.5 mm (1.7°)** ~ 6000	**1–2 mm** (3.5°–6.9°) ~ 5500	**2.5 mm** (8.7°) ~ 5500	Difference between modality: density up to 3000 cells/mm^2, cell-to-cell spacing up to 4 µm
Liu, 2019[26]	AO-OCT								**7°**		
		7	33.1	21–49		23.6–25.4			4834		RPE cell spacing (7°): 13.6 ± 1.1 µm
Granger, 2018[29]	IR and SWAF-AOSLO						**0–0.25 mm** (0°–0.9°)			**3.2–3.6 mm** (11° - 12.5°)	RPE cell visualization with IRAF, with lower cell contrast than with SWAF
		10	39.5	23–65	24.0	22.5–25.5	6026 ± 1590			T: 4552 ± 1370 (ns)	
		7	30.4	23–41			5898 ± 683			T: 3900 ± 439	No density change with age
		3	60.7	55–65			6883 ± 1629			T: 5741 ± 156	
Grieve, 2018[32]	NIR-AF-757						**0°**			**10°**	
		4	35.0	24–53			6250			4410	
Liu, 2017[28]	AO-NIR						**0°**	**0.5 mm** (1.7°)	**1- 2 mm** (3.5° - 6.9°) #	**2.5–5 mm** (8.7°–17.4°) #	
		10	27.3	22–40	23.4	22.1–24.7	6504 ± 604	6474 ± 331	6012 ± 320 (***)	5772 ± 293 (***)	RRS: 12.6 µm (fovea) - 17.8 µm (5 mm)
Liu, 2016[24]	AO-OCT							**3° T**	**7° T**		RRS: 12.2 - 15.5 µm (3°)
		6	39.3	25–61	24.6	23.6–26.1		4975 ± 651	4780 ± 354 (***)		Number of nearest neighbors: decrease in cell regularity with age
Tam, 2016[27]	AO-ICG + multimodal AO-SLO: confocal reflectance, split detection, dark-field	3	33	25–40				**1°–1.4°** 5811 ± 654			
Scoles, 2013[23]	dark-field AO-SLO	7		19–40			-	-	-	-	Nearest neighbor distance : 10.7±0.9 µm (center of fixation) - 13.4±0.6 µm (10°)
Morgan, 2009[22]	AF AO-SLO						-	-	**5°–7.5° #**	**8.75°–16.25° #**	RPE cell size and spacing increased with eccentricity
		3	27	25–30	N/A				5645 ± 403 (ns)	4609 ± 1175 (ns)	

Eccentricity expressed in mm are estimated in degree, assuming a 24-mm emmetropic eye with 0.288 mm/degree.[47] **#** Mean of average density per subject in the specified eccentricity range were calculated. (Level of significance of Unpaired *t* test with Welch's correction: ***, $P < 0.001$; ns, non-significant). Boldface indicates eccentricity ranges.

N/A = raw data not available; AF = autofluorescence; AO = adaptive optics; CoV = coefficient of variation; ICG = indocyanin green; IR = infrared; IRAF = infrared autofluorescence; NIR = near-infrared; RPE = retinal pigment epithelium; RRS = row-to-row spacing; SD = standard deviation; SLO = scanning laser ophthalmoscope; SWAF = short-wavelength autofluorescence; T = Temporal; TOPI = transscleral optical imaging.

Table 4B. Summary of Ex Vivo RPE Cell Imaging Studies in Healthy Eyes. For Comparison, the Reported Data from the Fovea to the Periphery are Summarized

Reference	Method (preparation)	Eye	Age (yrs)		Postmortem	Density (cells/mm²): Mean ± SD per Eccentricity Range			Other Cell Features reported	Effect of Age on RPE Cell Features
		N	*Mean*	*Min - Max*	*Time (H)*	*Fovea/Macula*	*Perifovea*	*Periphery*		
Bhatia, 2016[14]	IHC: cytoskeleton, nuclei (flatmount)					**∅ 0.5 mm** (∅ 1.7°)			Area, number of neighbors, eccentricity (~ elongation), form factor (~ circularity), polygonality (~ solidity)	Decreased density (0.54% / yr), higher cell area, higher eccentricity, and lower form factor with age
		14	58.8	29–80	< 7	4960 ± 1040				
		4	40.5	29–54		5662				
		10	71	62–80		4499				
Ach, 2014[13]	BAF, IHC: cytoskeleton (flatmount)				< 4.2	**0–0.6 mm** (< 2.1°)	**0.6–3 mm** (2.1° - 10.4°)	**> 3 mm** (10.4°)	Area, number of neighbors	RPE cell rearrangement throughout life
		10	39.9	16–51		6174 ± 1033	4847 ± 681 (***)	4473 ± 592 (ns)	Lipofuscin fluorescence	Fovea: no change with age
		10	84.8	82–90		6209 ± 1273	5300 ± 844 (***)	4527 ± 665 (ns)		Perifovea: increased density with age
Del Priore, 2002[48]	IHC: nuclei, TUNEL (flatmount)				14–24	**1.5 mm** (5.2°)	**1.5–3 mm** (5.2° - 10.4°)	**3–12.5 mm** (10.4°–43.4°)		Macula: no change with age
		22		19–84		4980 ± 90	4857 ± 75	4068 ± 207	Cell death	Periphery: decrease with age
Harman, 1997[12]	Light microscopy	21		12–89	N/A				Total cell number	High variability between subjects
										No change with age
Panda-Jonas, 1996[11]	Light microscopy (punches)				8.0 ± 2.8	**∅ 3 mm** (∅ 10.4°)		**2–5 mm** (6.9° - 17.4°)		Macula: decreased density with age (0.3% / yr)
		25	58.6	18–85		4220 ±727		3480 ± 466 (ns)		
Watzke, 1993[10]	Light microscopy (flatmount)				N/A	**∅ 0.5 mm** (∅ 1.8°)		**4 mm** (13.9°)		
		10	30.4	13–47		5893 ± 809		4834 ± 764 (**)	(n = 10 eyes) area, shape factor (~ circularity), polymegathism	Decreased density with age, only in fovea
		10	77.1	54–96		5327 ± 719		4769 ± 809 (*)		Loss hexagonality with age in fovea
Gao, 1992[9]	Light microscopy (en face section)				< 1–3	**1 x 2 mm** (3.5 × 6.9°)				
		35	55.4	17–95		7452 ± 661 (n = 22)				No change with age
Feeney-Burns, 1990[8]	Light microscopy (vertical section)					**0.6 mm** (2°)	**Macula**		Lipofuscin fluorescence	
		8	58.9	49–68	2–24	52.2 ± 4 cells/600 µm	85.1 ± 6 cells/mm; 44.2 ± 5 nuclei/mm		Nuclear spacing, cell width, cell height	Macula: decreased cell number with age
		14	93.7	90–101	2–39	37.4 ± 16.5 cells/600 µm	64.5 ± 3 cells/mm; 30 ± 11 nuclei/mm			
Dorey, 1989[7]	Light microscopy (vertical section)	19	47.2	(6 w–88)	< 12	**Macula**				Macula: decreased cell number with age
		15	> 20			8.1 ± 3 cells/90 µm = 90 cells/mm				

Eccentricity expressed in mm are estimated in degree, assuming a 24-mm emmetropic eye with 0.288 mm/degree.[47] (Level of significance of Unpaired *t* test with Welch's correction: *, $P < 0.05$; **, $P < 0.01$; ***, $P < 0.001$; ns, nonsignificant). Boldface indicates eccentricity ranges.

BAF = blue auto-fluorescence; IHC = immuno-histochemistry; N/A = not available; RPE = retinal pigment epithelium; SD = standard deviation; TUNEL = Terminal deoxynucleotidyl transferase dUTP nick end labeling.

the choriocapillaris[43] and concentration of melanin granules in the choroid behind the fovea.[44]

Only one-third of the subimages were selected because of the low contrast on RPE cell border in some areas together with the strict criteria applied to keep only high-quality data to use the Voronoi algorithm. Most of these high-quality subimages were located between 3° and 8° of eccentricity. In our Voronoi diagrams, we assumed a convex shape. The resulting diagrams presented a honeycomb mosaic that is consistent with the mosaic of healthy RPE cells, allowing the diagrams to estimate the RPE's morphologic features. When using the diagrams to compute the number of neighbors around each RPE cell, we obtained a value of 5.68 ± 0.11 (range 5.3−5.8), which is very similar to the value reported by Ortolan et al in the macular region (5.56 ± 0.35) in ex vivo human retina with a method to define the borders of each cell different from the Voronoi method.[45] The distribution of the number of neighbors is also coherent with the studies in which Voronoi was used to determine cell shape.[13,24]

The average CoV of all the cell features, measured in areas imaged multiple times, was < 4%, demonstrating the good repeatability of image acquisition with TOPI.[46] The literature analysis shows that depending on the in vivo imaging modality (Table 4A), the histologic methods (Table 4B), the populations, and the retinal locations, results of human RPE cell density may vary significantly, which makes the comparison with our results not trivial. Taking this into account, in the perifovea, the RPE densities that we have measured are lower than some in vivo[24,28] and ex vivo[13] measurements but consistent with our previous data[35] and those of Morgan et al.[22] In the periphery, the measured densities are lower than some in vivo[28] and ex vivo[10] measurements and consistent with those obtained in vivo by Morgan et al[22] and Granger et al [29] and ex vivo by Panda-Jonas et al[11] and Ach et al.[13] The measured RPE cell spacings are in agreement with the previously reported values.[24,28,29,35]

The RPE's morphologic features were then correlated with eccentricity, age, and AL. The results confirmed the regularity of the RPE mosaic in a narrow range of eccentricities in the macula and showed variability of RPE features between participants, related to the wide range of ALs and ages of the population included in the study. Eye elongation was significantly associated with a decrease in RPE cell density (implying an increase in cell area) without morphologic change. These results do not corroborate with the ex vivo studies of Jonas et al,[49] who reported that axial elongation is associated with a decrease in RPE cell density from or posterior to the equator, whereas RPE density in the macular region is independent of AL. There are many factors that could explain the change in the size of the macular RPE cells, including mechanical stress resulting from the activity of subfoveal smooth muscle cells fibers that are involved in the focalization process.[50,51] In pathologic myopia, posterior staphyloma develops in the posterior pole and not at the periphery, demonstrating that major alterations of all retinal layers might take place in the macula and not only in the periphery of myopic eyes. The observed changes in RPE cell density in the larger eyes are a new finding that needs to be confirmed in highly myopic eyes (< -6 D) and in a larger population.

Regarding the effect of age, in a previous set of data,[35] from 11 healthy volunteers of younger age (28 ± 9 years), we reported a higher mean RPE density decreasing with age (R^2 = 34%). The present study, conducted on a larger number of older participants, confirms that aging is slightly but statistically associated with a reduction in macular RPE cell density and further shows that it is associated with a change in cell morphology. The published results on the influence of aging on RPE cell density in the macula of normal human eyes are highly variable. Two in vivo studies reported no change in RPE density with aging, but participants ≥ 50 years old were only 4 out of 23 in the study by Baraas et al[25] and 3 out of 10 in the study by Granger et al[29] (Table 4A). Data from larger samples, acquired on postmortem donor eyes, have reported divergent results (Table 4B). One study found unchanged RPE density in the fovea and increased RPE density in the perifovea with age,[13] whereas others found stable[9,10,12,48] or decreased density in the macula[7,8,11,14] and the posterior pole.[52]

Finally, since the study by Watzke et al, which reported a loss of hexagonality with age in the fovea,[10] 3 studies have explored the morphometry of RPE cells. Ach et al[13] examined ex vivo the regularity of RPE cells from 20 donors (10 were < 51 years of age) and showed that the number of cells with 6 neighbors significantly decreases with age in the fovea and periphery, indicating that rearrangement of RPE cells occurs throughout life. With the same Voronoi-based metric, a slight decrease in cell regularity with age was also reported in vivo by Liu et al in 6 participants aged 25 to 61 years.[24] Our results regarding the distribution of the average number of neighbors per subimage also showed a decrease in the prevalence of 5.8 nearest neighbors from 35% (< 50 years) to 20% (> 50 years), confirming the rearrangement of RPE cells with aging. Our results are consistent with those of Bhatia et al,[14] who described a decrease in RPE cell density with age in healthy macula from 10 donors aged 29 to 80 years as well as changes in RPE cell morphometry. They computed shape and eccentricity factors that can be compared with our circularity and border distance CoV factors, respectively, and reported that macular RPE cells had larger area, more elongated shape, and were less symmetrical with age. The RPE cell features analyzed in vivo in the present study correlate with features analyzed on postmortem human RPE samples. Together with the repeatability measurements, the results constitute evidence toward reliability of the method.

Adaptive optics -SLO-based systems can image the RPE with different modalities, such as dark-field, OCT, near-infrared (NIR)-autofluorescence (AF), and enhanced indocyanin green. The flexibility offered by these methods allows for multiple perspectives of the RPE mosaic depending on contrast mechanisms based on reflectance or fluorescence.[31] Oblique flood-illumination used in TOPI uses a different contrast mechanism, namely, transillumination generated by backscattering, to image the RPE cells, thus offering a new perspective of the cells and their environment. Compared

with AO-SLO systems, the design of our TOPI instrument has a similar lateral resolution but provides a larger FOV (5° × 5°), corresponding to the largest FOV an AO system can acquire in a single acquisition. Moreover, TOPI needs lower radiant exposure than AO-SLO systems,[35] that is 3 orders of magnitude lower than that imposed by the American National Standards Institute norms on maximum permissible exposure. This is an important advantage of our method given the alarming evidence of hazards when imaging in the NIR at exposures 4 to 5 times lower than the current safety limits, as revealed by long-term reduction of NIR-AF.[33]

A few limitations were observed in our study. First, stability of fixation has not been measured, for example, by microperimetry, and differences between the PRL and anatomical foveal landmarks were not investigated. It has been reported that flood-illumination AO ophthalmoscopes for photoreceptor imaging exhibit, in healthy subjects, deviation of the PRL from 50 μm (equivalent to ∼ 0.15°) compared with the location of peak cone density[53] to an average of 0.85° compared with the foveal pit center.[54] In our study, participant fixation and low-resolution fundus visualization in our prototype allowed us to localize the fovea and check the approximate eccentricity accordingly. Second, the measurements performed with the prototype tested in this study acquired only one-third high-contrast images of the RPE cells and did not image RPE foveal cells with sufficient accuracy. Improvements in the hardware and software of the next version of the camera, the details of which are beyond the scope of this study, are expected to improve the contrast on the RPE cells and to acquire images of the cells in the foveal center. Finally, another limitation is the relatively low number of participants. Although the current study provides a large quantitative and qualitative analysis of human RPE cells, performed in vivo in healthy volunteers, larger homogeneous patient populations are necessary to enrich the normative quantitative data and subsequently describe pathologic situations.

Because TOPI allows for fast image acquisition and is user-friendly, it should provide new insights into RPE cells in normal conditions, identify early RPE changes that might predispose one to retinal diseases, and identify objective surrogate morphological RPE markers to test new therapies for retinal degenerative diseases.

Acknowledgment

This study is part of the ASSESS (retinAI phase contrast imaging for Early diagnoSiS) project that has received funding from EIT Health. EIT Health is supported by the European Institute of Innovation and Technology (EIT), a body of the European Union that receives support from the European Unions Horizon 2020 Research and innovation program.

Footnotes and Disclosures

Originally received: December 21, 2021.
Final revision: October 10, 2022.
Accepted: October 12, 2022.
Available online: October 19, 2022.Manuscript no. XOPS-D-21-00247R2.

[1] Laboratory of Applied Photonic Devices, School of Engineering, École Polytechnique Fédérale de Lausanne, Lausanne, Switzerland.

[2] Faculty of Biology and Medicine, University of Lausanne, Lausanne, Switzerland.

[3] Jules-Gonin Eye Hospital, Fondation Asile des aveugles, Lausanne, Switzerland.

[4] Centre de Recherche des Cordeliers, Université Pierre et Marie Curie, Paris, France.

[5] INSERM U1138, USPC, Université de Paris-Cité, Sorbonne Université, Paris, France.

[6] Assistance Publique - Hôpitaux de Paris, Ophtalmopôle, Cochin Hospital, Paris, France.

[7] Université Paris Cité, Paris, France.

[8] Hôpital Foch, Suresnes, France.

OSA Biophotonics Congress: Optics in the Life Sciences, 2021 (Virtual event).

Association for Research in Vision and Ophthalmology (ARVO) annual meeting 2021 (Virtual event).

Disclosure(s):

All authors have completed and submitted the ICMJE disclosures form.

The authors made the following disclosures: A.I.: Support − ARVO Travel Grant.

C.M.: Support − European Institute of Innovation & Technology (EIT) Health; Royalties or Licenses − Inventor of the Technology, Ecole Polytechnique Fédérale de Lausanne (EPFL); Patents − Three patent applications for the technology; Stock − Earlysight.

F.B.C.: Stock − Earlysight.

I.M.: Funding − EIT Health.

L.K.: Funding − EPFL, EIT Health, Innosuisse.

M.K.: Support − Earlysight, EIT Health; Royalties or licenses − Inventor of the technology, EPFL; Patent − Three patent applications, Earlysight; Stock − Earlysight.

R.D.: Grants − Earlysight.

T.L.: Support − Earlysight, EIT Health; Royalties or licenses − Inventor of the technology, EPFL; Patent − Three patent applications, Earlysight; Stock − Earlysight.

The other authors have no proprietary or commercial interest in any materials discussed in this article.

Supported by EIT Health (retinAI phase contrast imaging for Early diagnoSiS, ASSESS), Innosuisse 56126.1, ANR-20-CE17-0034, UNADEV MR-A-MD, The Abraham J. & Phyllis Katz Foundation.

HUMAN SUBJECTS: Human subjects were included in this study. This study (ClinicalTrials.gov: NCT04398394; kofam.ch: SNCTP000003921) was designed in accordance with the tenets of the Declaration of Helsinki, good clinical practice defined by the International Council for the Harmonization of Technical Requirements for the Registration of Pharmaceuticals for Human Use or the ISO 14155, as well as all national legal and regulatory requirements. The Ethics Committee of the Swiss Federal Department of Health approved the study (Authorization CER-VD no. 2019-00429). Written informed consent was received from all participants before inclusion.

This study (ClinicalTrials.gov: NCT04398394; kofam.ch: SNCTP000 003921) was designed in accordance with the tenets of the Declaration of Helsinki, good clinical practice defined by the International Council for the

Harmonization of Technical Requirements for the Registration of Pharmaceuticals for Human Use or the ISO 14155, as well as all national legal and regulatory requirements. The Ethics Committee of the Swiss Federal Department of Health approved the study (Authorization CER-VD no. 2019-00429). Written informed consent was received from all participants before inclusion.

No animal subjects were used in this study.

Author Contributions:

Conception and design: Kowalczuk, Kunzi, Gryczka, Mantel, Behar-Cohen, Laforest, Moser

Data collection: Kowalczuk, Kunzi, Iskandar, Misutkova, Gryczka, Navarro, Jeunet, Mantel, Laforest, Moser

Analysis and interpretation: Kowalczuk, Dornier, Kunzi, Iskandar, Misutkova, Navarro, Jeunet, Mantel, Behar-Cohen, Laforest, Moser

Obtained funding: Kowalczuk, Mantel, Behar-Cohen, Laforest, Moser

Overall responsibility: Kowalczuk, Mantel, Behar-Cohen, Laforest, Moser

Abbreviations and Acronyms:
AF = autofluorescence; **AL** = axial length; **AO** = adaptive optics; **BCVA** = best-corrected visual acuity; **CCS** = center-to-center spacing; **CoV** = coefficient of variation; **D** = diopters; **FOV** = field of view; **IOP** = intraocular pressure; **NIR** = near-infrared; **PRL** = preferred retinal locus; **QC** = quality criterion; **RE** = refractive error; **RPE** = retinal pigment epithelium; **SD** = standard deviation; **SLO** = scanning laser ophthalmoscope; **TOPI** = transscleral optical imaging.

Keywords:
Healthy volunteers, Retinal Pigment Epithelium, Adaptive Optics Transscleral Flood Illumination, High resolution retinal imaging.

Correspondence:
Laura Kowalczuk, PhD, École Polytechnique Fédérale de Lausanne, School of Engineering, Institute of Electrical and Micro-engineering, Laboratory of Applied Photonics Devices, BM 4127, Station 17, CH-1015, Lausanne, Switzerland. E-mail: laura.kowalczuk@epfl.ch.

References

1. Lakkaraju A, Umapathy A, Tan LX, et al. The cell biology of the retinal pigment epithelium. *Prog Retin Eye Res*. 2020: 100846.
2. Khan KN, Mahroo OA, Khan RS, et al. Differentiating drusen: Drusen and drusen-like appearances associated with ageing, age-related macular degeneration, inherited eye disease and other pathological processes. *Prog Retin Eye Res*. 2016;53:70−106.
3. Simó R, Villarroel M, Corraliza L, et al. The retinal pigment epithelium: something more than a constituent of the blood-retinal barrier–implications for the pathogenesis of diabetic retinopathy. *J Biomed Biotechnol*. 2010;2010: 190724.
4. Rothschild PR, Salah S, Berdugo M, et al. ROCK-1 mediates diabetes-induced retinal pigment epithelial and endothelial cell blebbing: contribution to diabetic retinopathy. *Sci Rep*. 2017;7: 8834.
5. Cheung CMG, Lee WK, Koizumi H, et al. Pachychoroid disease. *Eye*. 2019;33:14−33.
6. Feeney-Burns L, Hilderbrand ES, Eldridge S. Aging human RPE: morphometric analysis of macular, equatorial, and peripheral cells. *Invest Ophthalmol Vis Sci*. 1984;25:195−200.
7. Dorey CK, Wu G, Ebenstein D, et al. Cell loss in the aging retina. Relationship to lipofuscin accumulation and macular degeneration. *Invest Ophthalmol Vis Sci*. 1989;30: 1691−1699.
8. Feeney-Burns L, Burns RP, Gao CL. Age-related macular changes in humans over 90 years old. *Am J Ophthalmol*. 1990;109:265−278.
9. Gao H, Hollyfield JG. Aging of the human retina. Differential loss of neurons and retinal pigment epithelial cells. *Invest Ophthalmol Vis Sci*. 1992;33:1−17.
10. Watzke RC, Soldevilla JD, Trune DR. Morphometric analysis of human retinal pigment epithelium: correlation with age and location. *Curr Eye Res*. 1993;12:133−142.
11. Panda-Jonas S, Jonas JB, Jakobczyk-Zmija M. Retinal pigment epithelial cell count, distribution, and correlations in normal human eyes. *Am J Ophthalmol*. 1996;121:181−189.
12. Harman AM, Fleming PA, Hoskins RV, Moore SR. Development and aging of cell topography in the human retinal pigment epithelium. *Invest Ophthalmol Vis Sci*. 1997;38: 2016−2026.
13. Ach T, Huisingh C, McGwin Jr G, et al. Quantitative autofluorescence and cell density maps of the human retinal pigment epithelium. *Invest Ophthalmol Vis Sci*. 2014;55: 4832−4841.
14. Bhatia SK, Rashid A, Chrenek MA, et al. Analysis of RPE morphometry in human eyes. *Mol Vis*. 2016;22:898−916.
15. Ach T, Tolstik E, Messinger JD, et al. Lipofuscin redistribution and loss accompanied by cytoskeletal stress in retinal pigment epithelium of eyes with age-related macular degeneration. *Invest Ophthalmol Vis Sci*. 2015;56:3242−3252.
16. Tarau IS, Berlin A, Curcio CA, Ach T. The cytoskeleton of the retinal pigment epithelium: from normal aging to age-related macular degeneration. *Int J Mol Sci*. 2019;20:3578.
17. Milam AH, Li ZY, Fariss RN. Histopathology of the human retina in retinitis pigmentosa. *Prog Retin Eye Res*. 1998;17: 175−205.
18. Shu X, Beckmann L, Zhang H. Visible-light optical coherence tomography: a review. *J Biomed Opt*. 2017;22:1−14.
19. Calvo-Maroto AM, Cerviño A. Spotlight on fundus autofluorescence. Clin Optom *(Auckl)*. 2018;10:25−32.
20. Roorda A, Zhang Y, Duncan JL. High-resolution in vivo imaging of the RPE mosaic in eyes with retinal disease. *Invest Ophthalmol Vis Sci*. 2007;48:2297−2303.
21. Gao W, Cense B, Zhang Y, et al. Measuring retinal contributions to the optical Stiles-Crawford effect with optical coherence tomography. *Opt Express*. 2008;16:6486−6501.
22. Morgan JI, Dubra A, Wolfe R, et al. In vivo autofluorescence imaging of the human and macaque retinal pigment epithelial cell mosaic. *Invest Ophthalmol Vis Sci*. 2009;50:1350−1359.
23. Scoles D, Sulai YN, Dubra A. In vivo dark-field imaging of the retinal pigment epithelium cell mosaic. *Biomed Opt Express*. 2013;4:1710−1723.
24. Liu Z, Kocaoglu OP, Miller DT. 3D imaging of retinal pigment epithelial cells in the living human retina. *Invest Ophthalmol Vis Sci*. 2016;57:OCT533−OCT543.
25. Baraas RC, Pedersen HR, Knoblauch K, Gilson SJ. Human foveal Cone and RPE cell topographies and their correspondence with foveal shape. *Invest Ophthalmol Vis Sci*. 2022;63:8.
26. Liu Z, Kurokawa K, Hammer DX, Miller DT. In vivo measurement of organelle motility in human retinal pigment epithelial cells. *Biomed Opt Express*. 2019;10:4142−4158.
27. Tam J, Liu J, Dubra A, Fariss R. In vivo Imaging of the human retinal pigment epithelial mosaic using adaptive optics

enhanced indocyanine green ophthalmoscopy. *Invest Ophthalmol Vis Sci*. 2016;57:4376−4384.
28. Liu T, Jung H, Liu J, Droettboom M, Tam J. Noninvasive near-infrared autofluorescence imaging of retinal pigment epithelial cells in the human retina using adaptive optics. *Biomed Opt Express*. 2017;8:4348−4360.
29. Granger CE, Yang Q, Song H, et al. Human retinal pigment epithelium: in vivo cell morphometry, multispectral autofluorescence, and relationship to cone mosaic. *Invest Ophthalmol Vis Sci*. 2018;59:5705−5716.
30. Vienola KV, Zhang M, Snyder VC, et al. Microstructure of the retinal pigment epithelium near-infrared autofluorescence in healthy young eyes and in patients with AMD. *Sci Rep*. 2020;10:9561.
31. Bower AJ, Liu T, Aguilera N, et al. Integrating adaptive optics-SLO and OCT for multimodal visualization of the human retinal pigment epithelial mosaic. *Biomed Opt Express*. 2021;12:1449−1466.
32. Grieve K, Gofas-Salas E, Ferguson RD, et al. In vivo near-infrared autofluorescence imaging of retinal pigment epithelial cells with 757 nm excitation. *Biomed Opt Express*. 2018;9:5946−5961.
33. Masella BD, Williams DR, Fischer WS, et al. Long-term reduction in infrared autofluorescence caused by infrared light below the maximum permissible exposure. *Invest Ophthalmol Vis Sci*. 2014;55:3929−3938.
34. Wynne N, Carroll J, Duncan JL. Promises and pitfalls of evaluating photoreceptor-based retinal disease with adaptive optics scanning light ophthalmoscopy (AOSLO). *Prog Retin Eye Res*. 2020;83:100920.
35. Laforest T, Künzi M, Kowalczuk L, et al. Transscleral optical phase imaging of the human retina. *Nat Photonics*. 2020;14:439−445.
36. Hammer M, Roggan A, Schweitzer D, Müller G. Optical properties of ocular fundus tissues–an in vitro study using the double-integrating-sphere technique and inverse Monte Carlo simulation. *Phys Med Biol*. 1995;40:963−978.
37. Latychevskaia T. Lateral and axial resolution criteria in incoherent and coherent optics and holography, near- and far-field regimes. *Appl Opt*. 2019;58:3597−3603.
38. Caetano Dos Santos FL, Laforest T, Künzi M, et al. Fully automated detection, segmentation, and analysis of in vivo RPE single cells. *Eye (Lond)*. 2021;35:1473−1481.
39. Tseng Q, Duchemin-Pelletier E, Deshiere A, et al. Spatial organization of the extracellular matrix regulates cell-cell junction positioning. *Proc Natl Acad Sci USA*. 2012;109:1506−1511.
40. Thévenaz P, Ruttimann UE, Unser M. A pyramid approach to subpixel registration based on intensity. *IEEE Trans Image Process*. 1998;7:27−41.
41. Pollreisz A, Messinger JD, Sloan KR, et al. Visualizing melanosomes, lipofuscin, and melanolipofuscin in human retinal pigment epithelium using serial block face scanning electron microscopy. *Exp Eye Res*. 2018;166:131−139.
42. Pollreisz A, Neschi M, Sloan KR, et al. An atlas of human retinal pigment epithelium organelles significant for clinical imaging. *Invest Ophthalmol Vis Sci*. 2020;61:13.
43. Bartol-Puyal FA, Isanta C, Calvo P, et al. Relationship between vascular densities of choriocapillaris and the whole choroid using OCTA. *Int Ophthalmol*. 2020;40:3135−3143.
44. Weiter JJ, Delori FC, Wing GL, Fitch KA. Retinal pigment epithelial lipofuscin and melanin and choroidal melanin in human eyes. *Invest Ophthalmol Vis Sci*. 1986;27:145−152.
45. Ortolan D, Sharma R, Volkov A, et al. Single-cell-resolution map of human retinal pigment epithelium helps discover subpopulations with differential disease sensitivity. *Proc Natl Acad Sci USA*. 2022;119:e2117553119.
46. Bartlett JW, Frost C. Reliability, repeatability and reproducibility: analysis of measurement errors in continuous variables. *Ultrasound Obstet Gynecol*. 2008;31:466−475.
47. Kolb H. Facts and figures concerning the Human Retina. 2005 May 1 [updated 2007 Jul 5]. In: Kolb H, Fernandez E, Nelson R, eds. Webvision: The Organization of the Retina and Visual System [Internet*]*. Salt Lake City, UT: University of Utah Health Sciences Center; 1995.
48. Del Priore LV, Kuo YH, Tezel TH. Age-related changes in human rpe cell density and apoptosis proportion in situ. *Invest Ophthalmol Vis Sci*. 2002;43:3312−3318.
49. Jonas JB, Ohno-Matsui K, Jiang WJ, Panda-Jonas S. Bruch membrane and the mechanism of myopization: a new theory. *Retina*. 2017;37:1428−1440.
50. Nickla DL, Wallman J. The multifunctional choroid. *Prog Retin Eye Res*. 2010;29:144−168.
51. Flügel-Koch C, May CA, Lütjen-Drecoll E. Presence of a contractile cell network in the human choroid. *Ophthalmologica*. 1996;210:296−302.
52. Ts'o MOM, Friedman E. The retinal pigment epithelium: III. Growth and development. *Arch Ophthalmol*. 1968;80:214−216.
53. Putnam NM, Hofer HJ, Doble N, et al. The locus of fixation and the foveal cone mosaic. *J Vis*. 2005;5:632−639.
54. Roshandel D, Sampson DM, Mackey DA, et al. Impact of reference center choice on adaptive optics imaging cone mosaic analysis. *Invest Ophthalmol Vis Sci*. 2022;63:12.